

3 3D Results

XT: add one more section as an individual file/chapter for 2D models description. Currently, we have three factors controlling the model behaviors. They are three ranges of M variation along the ridge axis ($0.5\sim0.7$; $0.5\sim0.8$; $0.2\sim0.8$), three functional forms of M variation (linear; sinusoidal; square root) and two types of weakening rate (Type 1 and Type 2) as described in detail in the section “Parameters to control”.

Generally, all models forms a median valley that deepens and widens toward the lower M side (Figure 8) except the reference model with constant $M= 0.8$ (Figure 11). The topography observed in our models, to the first order, is controlled by the spatial and temporal distributions of faulting and to the second order, results from elastically deformation (e.g. The gradual deepening and widening of the median valley; The bending of the crust at the footwall side of the detachment fault results in a domal shape of the fault interface as a mechanism for producing the dome shape of OCCs).

The pattern of the deformation (faulting and elastic deformation) is controlled by the evolving stress in the crust in terms of its distribution and magnitude. The stress evolution is a result of the interaction processes between tectonics and magmatism. Due to constant seafloor spreading, tensional stress orthogonal to the ridge-axis in the crust keeps accumulating. At the same time, along ridge-axis varying diking partially accommodates the stress from far field extension and perturbs the homogeneity state of stress distribution along the ridge-axis. Accumulated stress will be largely released when the normal or shear failures establish.

In this “Results” chapter, we will first describe in detail the model behaviors of two reference models. Then, we will compare the reference model and the other data points with different setup parameters. Formation mechanism will be explained mostly in this chapter and will be further discussed and compared with nature observation in the “Discussion” chapter.

3.1 Reference models

We consider two models as our reference models: one, M varies linearly from 0.2 to 0.8 along the ridge axis with increasing Z; two, constant M along the ridge axis as a comparison to the changing M models.

3.1.1 M varies along the ridge-axis (M28LinT1 Table 1)

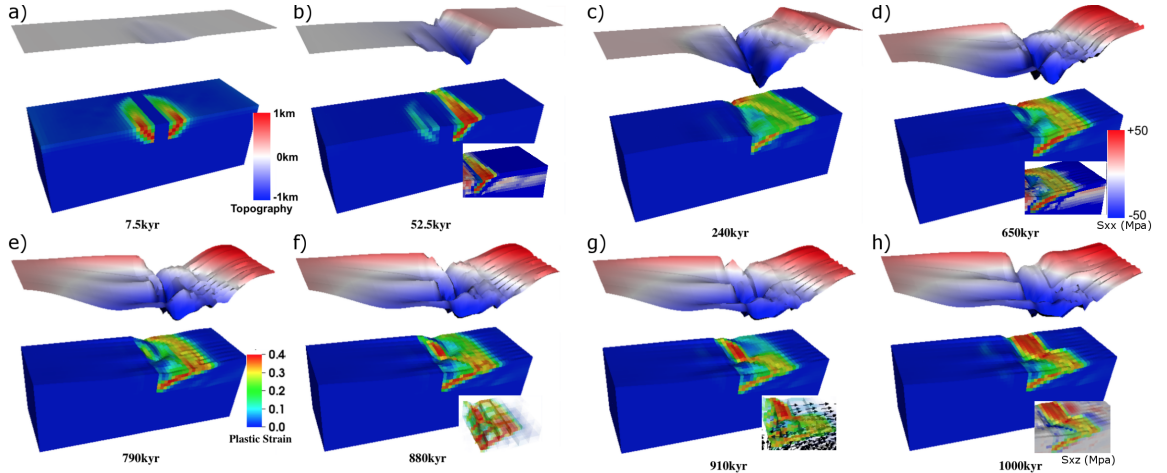


Figure 8: Reference model one: M linearly increases from 0.2 to 0.8 from front to back, Type one weakening (M28LinT1) (Table 1). The top layer is the topography of the model with five times vertical exaggeration. The color scale within Figure 8.a is for the topography. Initial seafloor is marked as a reference of zero km in height. The green, yellow and red colors in the background of blue model domain are plastic strain. Its color scale is shown in Figure 8.e. The number with kyr as a unit beneath each model result is the time for the model with a unit of thousands of year. The two insets in Figure 8.b and Figure 8.d is for stress σ_{xx} (Sxx in the figure). Positive value (pink and red) means tension and negative (blue) is compression. The inset in Figure 8.h is for shear stress σ_{xz} (Sxz in the figure). It share the same color scale with insets in the Figure 8.b and Figure 8.d. The inset in Figure 8.f is a transparent view of plastic strain. The inset in Figure 8.g shows both plastic strain and the velocity vector. Indicated by the velocity vector, the hanging wall of the detachment fault at low M region ($M0.2\sim M0.5$) is moving in an opposite direction to the hanging wall at higher M region ($M> 0.5$).

As shown in Figure 8, the model creates a median valley that both widens and deepens through time and the rate of its widening and deepening at a specific location (in terms of Z-axis) is inverse proportional to the rate of local magma supply (i.e. M value). OCCs with more than one kilometer in relief and tens of kilometers in wavelength are produced

in the model. One interesting behavior worth noting is that corrugations with hundred-to-kilometer wavelengths are also produced by the model.

As shown in Figure 8.a, in the first 7.5kyr, high angle ($\sim 60^\circ$) (consistent with Anderson's theory of faulting mechanics for a frictional angle of 30°) normal faults (shown as higher plastic strain shear bands with a thickness of 2~4 times of the width of a single hexahedron element) begin to form near the ridge axis in terms of plastic strain localization near the ridge center (weakest place to initiate a fault), because of the thickness of the crust is thinnest at the ridge center due to our thermal structure setup. For each timestep, the tensional stress accumulates faster at the lower M side where the crust reaches a yielding point earlier than higher M side and so the fault first initiates at the front (lower M side) and then propagates to the back (higher M side). However, the along ridge-axis coupling (internal strength preventing relative displacement (i.e. rotation, offset) between two neighbors along the Z-axis) assists in fault propagation from front to back and reduces the time difference in initiation of faulting along the ridge-axis ^{XT:}when comparing with separate 2D models [It probably will be verified after a 2D results analysis and conclusion].

At 52.5kyr (Figure 8.b), the normal fault on the right hand side of the ridge axis continues to evolve while the one on the left becomes inactive. The choice of which fault will develop is a random event since the model setup is symmetrical across the ridge-axis. The timing difference of initiation of faulting along the ridge axis creates an offset in X-axis direction between along ridge-axis breakways that the breakaway at the lower M side extends further than that of the higher M side (Figure 10). This offset remains constantly around three elements until time 295kyr (Figure 10.d) because the extending velocity of the breakaway to move away from the ridge-axis is only controlled by the far field extension rate, V_x . ^{XT:}Why after 295kyr the offset reduces needs to be answered. I don't know now.
Probably partly due to healing that earlier the fault initiation, more healing it experiences.

In addition, as shown in the inset of (Figure 8.b) with status of σ_{xx} distribution, as the fault offsets, crust at the footwall begins to bend in a clockwise rotation (view from front)

(Figure 18) and the neutral plane ($\sigma_{xx} = 0$) is shown as the boundary between blue (compression) and pink (tension). In the “Discussion” section, we will show that this bending force created in the crust of footwall together with fault weakening as a trade-off factor is essential for faulting evolution. ^{XT:}Delete this add after finish discussing the bending force and weakening effect.

The location of the termination of the detachment fault where footwall begins to be exhumed to the surface varies along the ridge-axis (i.e. Z-axis). As shown in Figure 9, the highest strain rate regions (red) can be interpreted as detachment fault interfaces. When $M \leq 0.5$, although the rate of fault slip should be higher for lower M, the rate of bending or decreasing in dip angle of the fault has a maximum value corresponds to the far field extension rate. Because for $M < 0.5$, the detachments root at the same place (center dike at a depth five to six elements beneath the surface)(Figure 9.Z=0, 5, 10) along the ridge-axis, the amount of bending in the footwall of the detachment is determined by the amount of the displacement of the breakaway. In other words, because in order to spend least frictional energy during faulting, fault interface between the two ends (breakaway and root) tends to be a straight line. Thus, the dip angle of the fault is inverse proportional to the distance between the breakaway and the root of the normal fault when $M < 0.5$. So the further between the breakaway and the root of the fault, the lower its dip angle. Since the breakaways at the region with $M < 0.5$ is pulled with the same velocity V_x , the distances between the breakaways and the roots of the faults are the same. Thus the dip angles of the faults at the same time along the ridge-axis are the same. However, when $M > 0.5$, the amount of fault slip decreases as M increase and the crust at the footwall experiences less bending and the detachment remains in high angle with closer to ridge-axis termination (Figure 9.Z=15, 20). This is due to the root of the fault is being slowly pushed away from ridge-axis while the breakaway of the fault is closer to ridge center since the fault initiates later than that at the low M side. In addition, the crust thickness that the fault cuts through is slowly increasing as the fault being pushed away from ridge center due to excessive diking.

These three factors together contribute to a higher dip angle. In a unit time, the volume of the exhumation is also smaller for the higher M side. One thing needs to be noted that the lowest topography points at high M side correspond to the terminations but detached from the terminations at the low M side ($M < 0.5$) as shown in Figure 9.

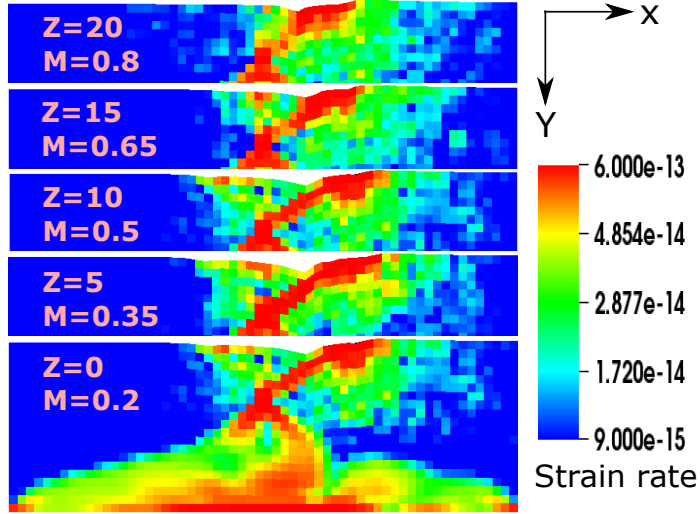


Figure 9: M28LinT1 (Table 1). Strain rate at 107.5kyr with five slices along ridge axis(Z axis).

At 240kyr (Figure 8.c), the median valley further deepens and widens. The detachment keeps active and extends to ~ 18 km in length horizontally (longest at $M = 0.2$) with the dip angle decreases from initially $\sim 60^\circ$ to 30° (at the root of the fault) and 0° where the fault interface is exposed to the seafloor. However, for the detachment at the higher M side (especially the last three elements along the Z-axis), the dip angle remains high. The maximum relief between highest point in breakaway and lowest point in the median valley becomes larger than 1km. Corrugations show up at the lower M side, at the front tip of the extending fault interface. The lowest topography points inside the median valley evolves from a straight line parallel to the ridge-axis (Figure 10.a) to a line oblique to the ridge-axis (Figure 10.b,c,d). Initially, the lowest topography points are at the terminations of the detachment fault. Due to the coupling along the ridge-axis, fault propagates from front to back in a straight line parallel to the ridge-axis. However, as the dip angle of the detachment at the low M side begin to decrease due to bending of the crust at the footwall, along with

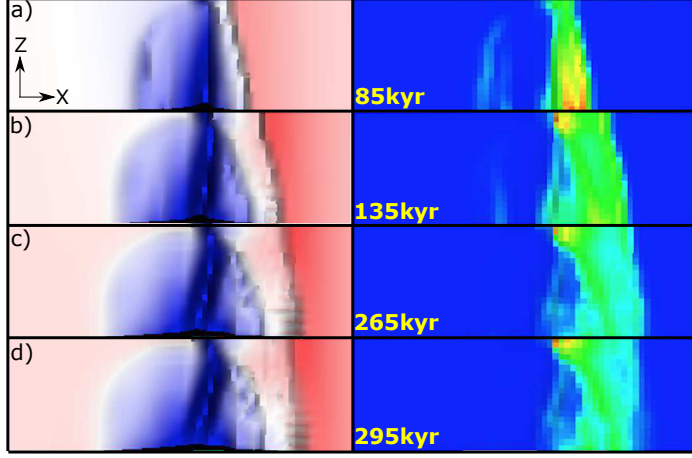


Figure 10: M28LinT1 (Table 1). Breakaway evolution through time. Viewing from top. Left column is topography at different time; Right column is plastic strain. They both share same color scales in the figure 8. The offset between breakways along the ridge-axis in X-axis direction remains three elements until time 295kyr. It also shows that the lowest topography points along the ridge-axis start as a straight line parallel with ridge-axis in a) and then gradually become oblique to the ridge-axis. Please see text for detail description.

excessive tensional stress results from low magma supply, the lowest topography point at the lower M side is pulled to the conjugate plate. While the lowest topography points at the high M side ($M > 0.5$) are pushed away from the dike. Note that the oblique lowest topography points form not a straight line, but a curve that the lowest point remains near the ridge-axis at the high M side. This is due to the bending rate of the detachment at high M side is very low and thus the termination can remain near the ridge-axis.

XT: One question needs to be answered: at 410 timesteps (205kyr), the breakaway at the front already extends 15km. If assuming a constant extending rate, it means a velocity of around 75km/Myr, much faster than half spreading rate 25km/Myr. If it is true, I need to change previous discussion on how fast breakaway being pulled away from ridge-axis.

At 650kyr (Figure 8.d), the median valley continues to deepen and widen. The breakaways along the ridge-axis already *XT:* moved out of the model domain [it should not, if breakaway move with 25km/yr(half spreading rate), since the distance between initial break (5km away from ridge center) and right wall of the model domain is about 25km which needs 1Myr to reach. But now is only 650kyr. Why is it?]. The fault offset is already

larger than the thickness of the crust and the upper mantle materials begin to be exhumed to the surface. The previous fault interface bend over to a negative dip angle (dip in an opposite direction) and produces a dome shape OCC with corrugations on its surface parallel to the spreading direction. The previous lowest topography points evolve to a curve with bigger curvature. Compared to the inset in Figure 8.b, the total length of the bending crust decreases. A hint of a near-axis secondary fault begin to initial at the high M side ($10 < Z < 15$) as a form of tension failure. ^{XT:}Its formation will be discussed in Discussion section accompanied by the stress status analysis.

At 790kyr (Figure 8.e), the initial tension failure immediately ajacent to the ridge center (hint of the secondary fault) begin to evolve and propagate to higher Z region.

At 880kyr (Figure 8.f), at the higher M side, the initial tension failure evolves to a high angle near-axis secondary normal fault and replace the initial detachment as indicated in the inset of transparent view of plastic strain.

At 910kyr (Figure 8.g), the secondary normal fault results in a strong constrast in moving directions between high M side and low M side near the ridge-axis that at the high M side, previous hanging wall becomes footwall and moves with spreading direction on the right, however, at the low M side, due to deficit in magma supply, the hanging wall is coupled with conjugate plate and moves to the left as shown in the inset. This opposite direction motion creates a strong shear stress region $\sim 45^\circ$ oblique to the ridge-axis (inset of Figure 8.h) and produces new lowest topography points align with it. Combined with previous lowest topography points, an “X” shape topography low is created.

Corrugations are observed in the model since 240kyr. It will be further discussed in the discussion chapter. There are two contributing factors, for one, trans-extenstional stresses are created due to offset of the breakaway as well as the variation in fault displacements along the ridge axis; for the other, the variation of the positions of the terminations of the detachment faults along the ridge-axis creates anastomosing faults that is mentioned in [Smith et al., 2014]. This anastomosing faulting behavior is largely responsible for

corrugations in our models.

3.1.2 Constant M along the ridge-axis

XT: This section needs to be revised and add more details into the model description. Another reference model is the model with constant $M = 0.8$ along the ridge axis as a comparison to the changing M models.

As shown in Figure 11, this constant M along the ridge-axis model creates a median valley of $\sim 20\text{km}$ in width and $1 \sim 2\text{km}$ in depth which is similar to generally observation of Mid-Atlantic Ridges. The width and depth of the median valley is almost constant along the ridge-axis. The variation along the ridge-axis in breakaway and termination as well as the existence of corrugation mentioned in reference model one are not observed.

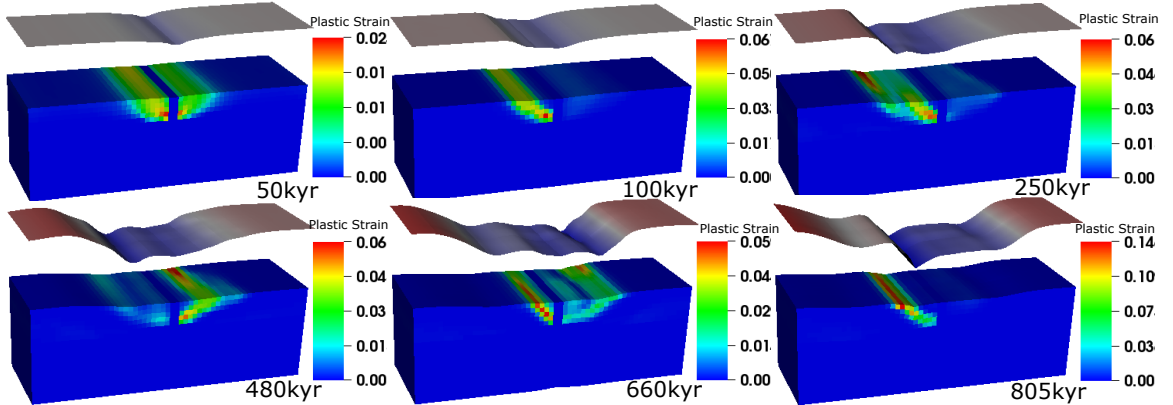


Figure 11: M88ConT2 (Table 1). Reference model two: constant $M = 0.8$ along the ridge-axis (i.e. Z axis). Type two weakening.

Based on the previous experience in pseudo-2D models or [Lavier et al., 2000], with higher characteristic fault offset (ΔX_c) for Type two weakening compared with Type one weakening, the frequency of normal faulting alternation is higher for $M > 0.5$ cases. However, interesting enough, when comparing pseudo-2D and 3D models when they are using Type two weakening under case of $M = 0.8$, even though the 3D Model has a larger ΔX_c of 1km than that of pseudo-2D model of 0.5km, 3D model has a lower frequency of faulting alternation. Since M is constant 0.8 along the ridge-axis, the effect of along ridge cou-

plingthat resists alternation need not be considered. One possibility is that the resisting bending force increase in a higher rate than linear with respect to increasing the length of the ridge segment (Z_{max} km).

3.2 Tables of all the data points

Currently, we have run ~~XT: hundreds of [find out exactly number that will be used in 2D model results conclusion]~~ Pseudo-2D models for initial setup and benchmarking with previous studies (e.g. [Buck et al., 2005] and [Tucholke et al., 2008]). Based on those Pseudo-2D models, we further ran 11+1 (11 models with M variation along the ridge-axis and 1 model with constant M= 0.8 along the ridge-axis) 3D models shown in Table 1. The available data points are limited due to the huge computation expenses for 3D models (For each model to be run to 2Myr, usually needs 192 cores for about 2 days (around 10000 SUs). ~~XT: use 96 cores can improve the efficiency a little bit (Longer time but smaller amount of SUs needed).~~)

Model	M range	Functional Form	Type of weakening	For short
1	M28	Linear	Type one	M28LinT1
2	M28	Sinusoidal	Type one	M28SinT1
3	M28	Square Root	Type one	M28SqrtT1
4	M57	Linear	Type one	M57LinT1
5	M57	Sinusoidal	Type one	M57SinT1
6	M57	Sinusoidal	Type two	M57SinT2
7	M57	Square Root	Type two	M57SqrtT2
8	M58	Sinusoidal	Type one	M58SinT1
9	M58	Sinusoidal	Type two	M58SinT2
10	M58	Square Root	Type one	M58SqrtT1
11	M58	Square Root	Type two	M58SqrtT2
12	M88	Constant	Type two	M88ConT2

Table 1: List of 3D numerical experiments

Based on the 11 models with M variation, we observed eight first-order behaviors as shown in Table 2.

A	Alternating Fault	C	Corrugation	SL	Shear Topography Low
NA	Not Alternating	SF	Secondary Fault on one side	CB	Cut Back
DD	Double Dome	AM	Atlantis Massif		

Table 2: Model behaviors in short.

M range Type \	M28	M57	M58
Type one	NA; C; SL; SF _{1500kyr} ; DD	NA; C; SF _{1380kyr} ; CB _{330kyr} ; AM(opposite z)	
Type two			

Table 3: Linear functional form.

M range Type \	M28	M57	M58
Type one	NA; C; SL; SF _{995kyr}	NA; C; SL; SF _{760kyr} ;1320kyr; CB _{520kyr} ; AM	NA; C; SL; CB _{510kyr} ; SF _{760kyr} ;1140kyr;1990kyr
Type two		NA; C; SL; SF _{680kyr} ; CB _{905kyr}	A _{450kyr} ;600kyr; C(only at low M); CB _{990kyr}

Table 4: Sinusoidal functional form.

M range Type \	M28	M57	M58
Type one	NA; C; SL; CB _{205kyr} ;330kyr;1025kyr		NA; C _{1770kyr} (due to shear with dif wave length); SF _{860kyr} (high M); SF _{1190kyr} (low M)(Dog Bone); SF _{1690kyr}
Type two		NA; C; SF _{435kyr} ;1060kyr; CB _{585kyr} ; CB _{735kyr} ; CB _{910kyr} ; CB _{970kyr}	A _{550kyr} ;920kyr; C; CB _{400kyr}

Table 5: Square root functional form.

Based on the available data points as shown in the tables, we are able to compare the model results with respect to three factors: 1) Variation of the range of M; 2) Variation of the functional form and 3) Influence of weakening rate.

3.3 Variation of the functional form

How magma supply varies along the MORs ridge-axis remains a current research question and we do not have direct quantitative observation over it. However, from indirect geo-physical studies (e.g. gravity, seismology), people suggest a general qualitative pattern of 20 to 50 km long second-order ridge segment with magma mostly supply at the segment center and decreases to the end [Carbotte et al., 2015]. Since we do not know exactly how magma supply varies along the ridge, we try three functional forms (linear, sinusoidal and square root) for its variation along the ridge-axis.

3.3.1 Comparing M28 in terms of linear, sinusoidal and square root

As shown in the tables, M28 with Type one weakening is the only M range that has three functional forms data points available. There are two phenomena that show distinct differences with respect to different functional forms. One is the geometry and timing of the secondary fault. The other is the “Cut back” behavior mostly observed in the square root model.

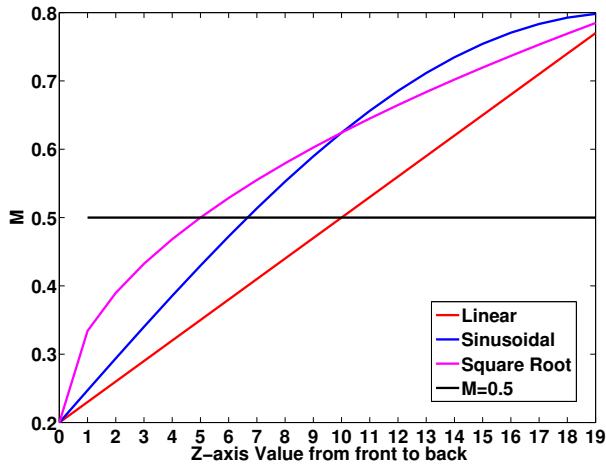


Figure 12: Three functional forms of M variation comparison. They begin to exceed the $M = 0.5$ black line at $Z=10, 7, 5$ for linear, sinusoidal and square root respectively.

Secondary Fault For linear, the secondary fault at higher M side begins to take place at around 900kyrs (Figure 13), its spatial distribution is at $M > 0.5$ region. It nucleates from the shear low (ridge center where $M = 0.5$) to the $M = 0.8$ end (Figure 12 where the red line begin to exceeds 0.5 at $Z = 10$). As it evolve, the initial detachment becomes inactive. This secondary fault creates another dome with initial composition likely to be volcanic rather than ultramafic, however, as it evolves, if it can last long enough to cut through the whole crust, mantle materials might exhumed to the surface. The composition of the domes observed at Kane magamullions is similar to this mechanism between ultramafic babel dome and eastern to it the crustal inside-corner high.

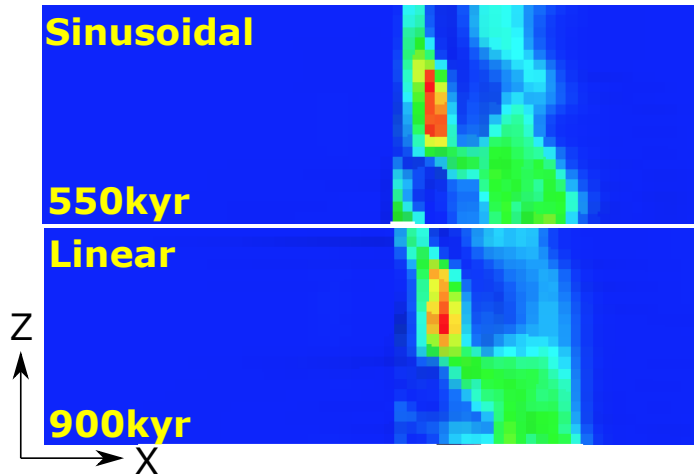


Figure 13: M28LinT1 versus M28SinT1 (Table 1). Secondary fault length comparison between linear and sinusoidal. Around 13 elements in length for sinusoidal compared to 11 elements for linear.

For sinusoidal, the secondary fault begins to form at a much earlier time around 550kyrs (Figure 13), this is due to the total area of $M > 0.5$ for sinusoidal functional form is higher than that of linear. Qualitatively, the total force to push the hanging wall of the detachment away from the dike for sinusoidal is larger than that of linear. The larger the force, the faster the detachment moves off axis, the earlier the secondary fault will appear. In addition, the total length of the secondary fault is longer due to the total length of M that is above 0.5 is bigger than that of the linear model (Figure 12). For square root, there is no secondary fault forming because the “cut back” behavior releases the tensional stress in the hanging

wall.

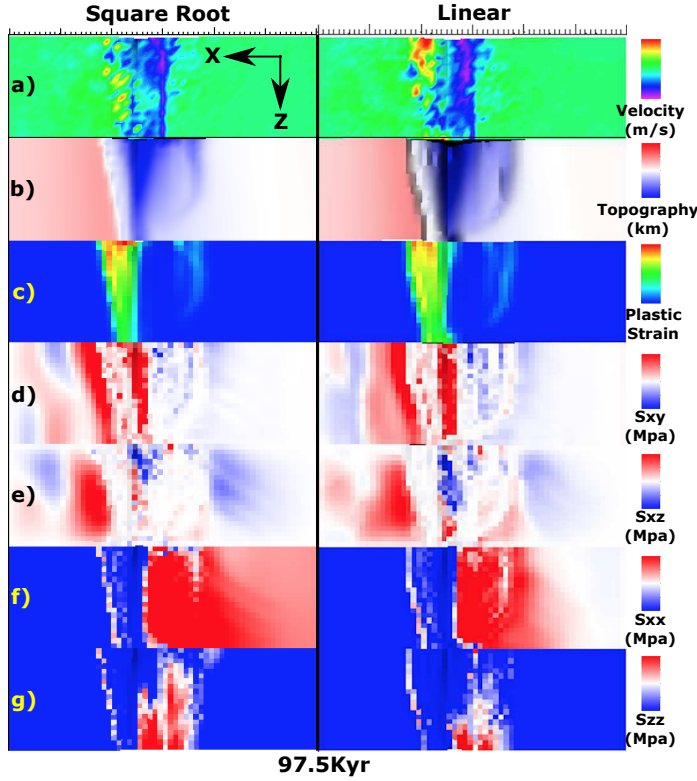


Figure 14: M28LinT1 versus M28SqrtT1 (Table 1) at 97kyr. View from top of the model.

Cut back The cut back happens mostly in the square root model. Since the linear model and the square root model have more obvious difference in terms of the cut back behavior, here, we only compare linear and square root. There are several factors contribute to the cut back behavior. First, at the higher M side, the amount of diking for the square root model is ubiquitously larger than that of the linear one (Figure 12). This leads to a slower bending detachment at the high M side for the square root model. Second, the total length of the ridge segment with $M > 0.5$ for the square root model is also longer than that of the linear one (Figure 12). This results in that at the low M side, σ_{xz} is focused at low Z adjacent to the ridge-axis (Figure 14.e), however for linear is spread out to Z higher than 10. Third, due to higher value of $\frac{dM}{dZ}$ for square root when $Z < 5$, the along ridge-axis shear σ_{xz} for square root will be accumulating faster, which produces larger strike-slip force to cut the

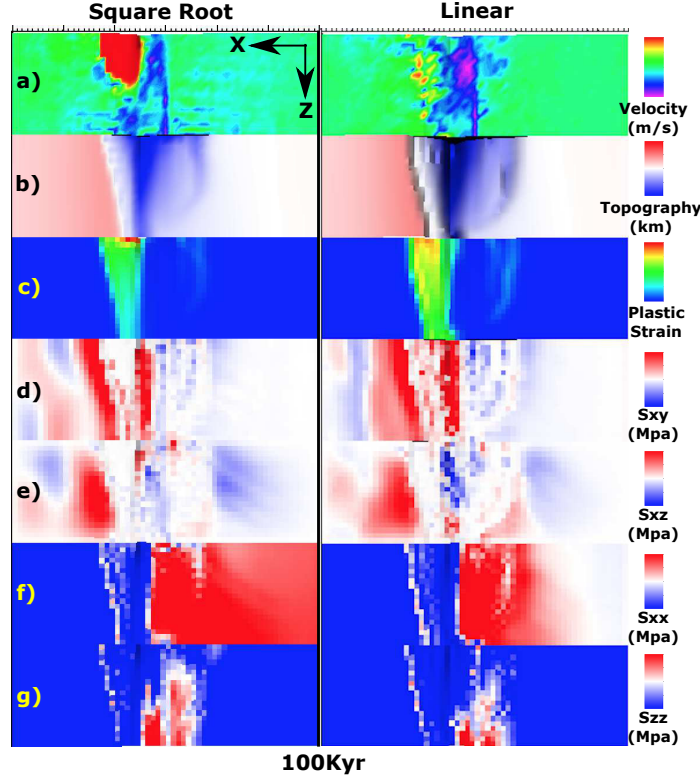


Figure 15: M28LinT1 versus M28SqrtT1 (Table 1) at 100kyr. View from top of the model.

hanging wall at the low M side. Fourth, as observed in the model (Figure 14.c), the parallel to spreading direction offset between breakaways along the ridge-axis is 4km for the square root model compared to 3km for the linear model. This causes the square root model to experience bigger shear stress σ_{xy} both immediately beneath and above the fault interface at the low M side (Figure 14.d). Fifth, as shown in Figure 18, due to bending of the crust at the footwall side, below the blue neutral plane, $\sigma_{xx} > 0$, meaning tensional stress being accumulated as fault develops. The resulting force tends to unbend the bended crust and drag down the connecting surface (the future decoupled hanging wall). All five factors together assist in the decouple of the hanging wall at the low M side as described in detail in the next paragraph.

In the Figure 16, the hanging wall rebounds backwards to the dike in a high velocity (Figure 16.b,e (velocity)) accompanied with a sudden topography drop (Figure 16.b) compared to c); d) compared to e) (in the second row)). This behavior is triggered when the

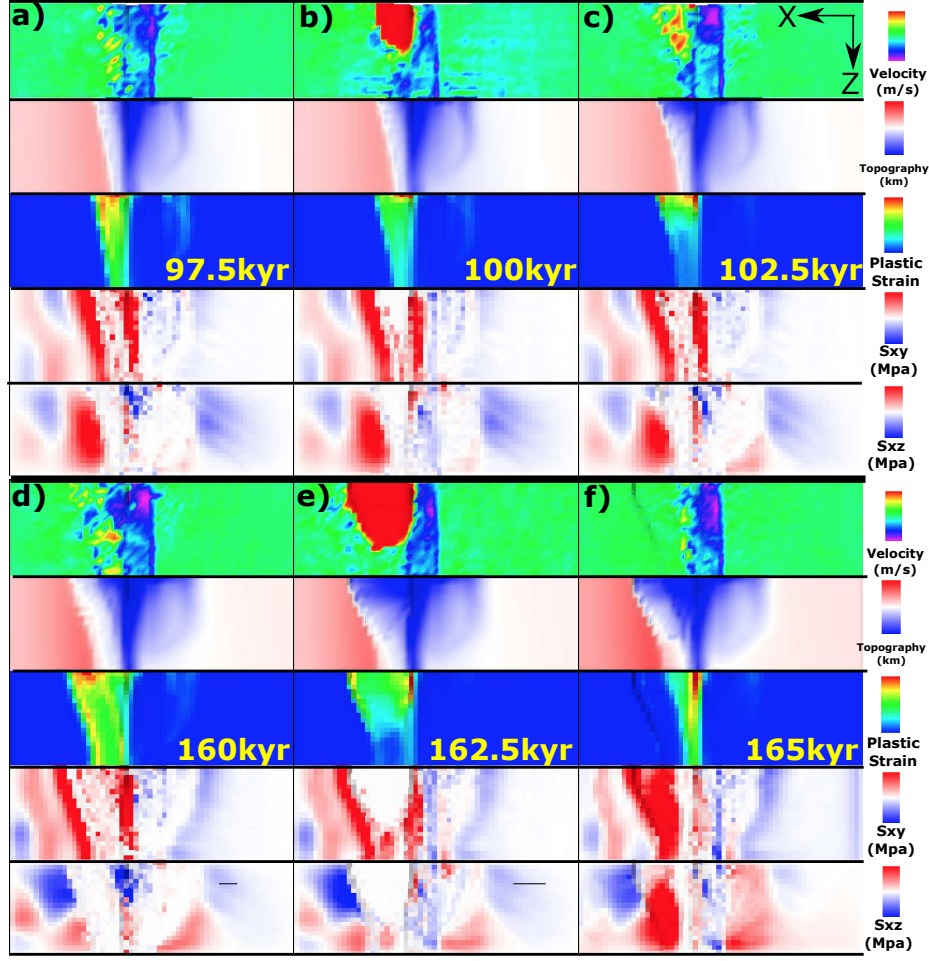


Figure 16: M28SqrtT1 (Table 1). Cut back behaviors in square root functional form model with different time.

front tip of the weak detachment extends further away from the ridge-axis and reaches a pre-accumulated shear zone (Figure 17). The pre-accumulated shear zone adds extra shear force to the weak (Figure 16.d(third row: plastic strain)) as well as shear stresses accumulated (Figure 16.d(fourth and fifth row: σ_{xy} and σ_{xz})) fault interface and together with the five factors mentioned in the previous paragraph result in the cut back behavior. The cut back produces a continuous high angle fault scarp with a relief of $\sim 1\text{ km}$ aligns to the initial breakaway and extends for about 20 kilometer in length (Figure 16.e (second row: topography)). Its distance to the ridge-axis varies along the Z-axis and this result can be used to indicate the magma supply variation in the nature as will be discussed in the “Discussion” chapter. ^{XT:}To be discussed, as a reminder

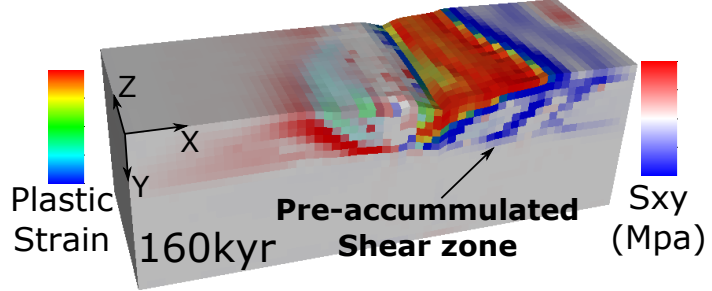


Figure 17: M28SqrtT1 (Table 1). Square root functional form model at 160kyr. Pre-accumulated shear zone increase the shear force and cut the weak detachment front tip

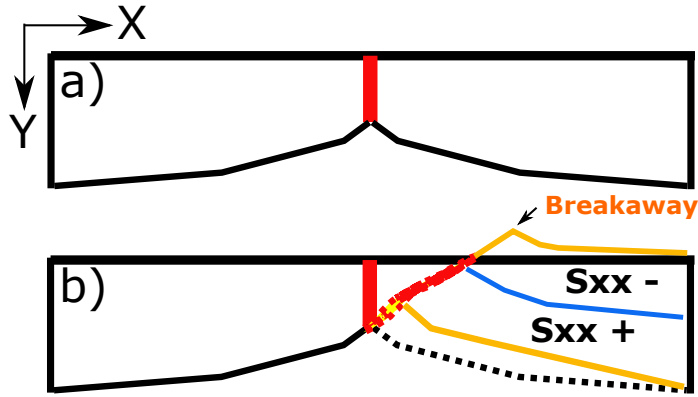


Figure 18: Bending stress illustration. The blue line is the neutral plane where $\sigma_{xx} = 0$. Above the neutral plane is compression and beneath it is tension. Due to sea water pressure and lithostatic pressure, compression is generally one degree magnitude larger than tension.

During the cut back process, the tensional bending stress are released at the low M side ($0 < Z < 7$) in the left tip of the bended crust (Figure 19.a compared to b), however, in the higher M side, the tensional bending stress keeps accumulating due to the far field extension (Figure 19.c compared to d). This behavior assists in the decouple between low M and high M side hanging walls.

Once the cut back happens at 162.5kyr, the σ_{xy} , σ_{xz} and σ_{xx} are released (Figure 16.e (fourth and fifth row: σ_{xy} and σ_{xz})). The plastic strain near the ridge-axis at low M side reaches a maximum of ~ 0.9 (Figure 16.e (third row: plastic strain)) compared to ~ 0.3 before and after. This is due to the sudden backward motion squeezes the end element of the hanging wall near the ridge-axis and later be released by the continuous extension.

After the cut back, the termination of the detachment recedes backwards for about 7

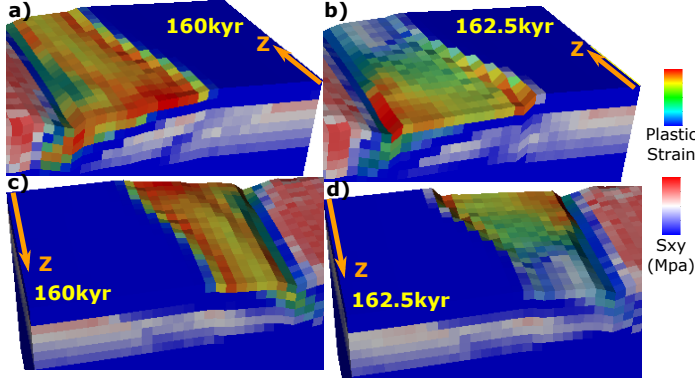


Figure 19: M28SqrtT1 (Table 1). Bending stress drop in the crust close to dike due to cut back behavior.

kilometer towards the ridge-axis (Figure 16.f (third row: plastic strain)) (termination fronts are always consistent with tension stresses in σ_{xx} and σ_{zz} as well as with plastic strain front(due to healing, high plastic strain region corresponds only to region with continuously deformation) (Figure 14 and Figure 15)). This behavior helps maintain a high angle normal fault. Different from the linear and sinusoidal models that the detachments at the low M side will rotate to a very low angle, square root model doesn't. In addition, σ_{xy} and σ_{xz} soon fill in the area between cut back created fault scarp and the new termination (Figure 16.f (fourth and fifth row: σ_{xy} and σ_{xz}) because σ_{xy} always accumulates immediately beneath the normal fault interface and the red σ_{xz} left to the new termination is due to the along ridge-axis variatioin in the rate of fault slip (low M side larger).

There is one phenomenon very interesting and counter-intuitive that worth describing here. After the cut back, and termination retreat, the evolution of the detachment fronts is opposite to initiall or to the general behavior in the linear and sinusoidal models. The termination front at the high M side extends faster and further after the cut back (Figure 20). This is partly related to the unbending decouple phenomenon we described ealier that the tensional stress are released at the low M side but continues to accummulate in the high M side which results from the cut back unbending in the low M side. Since the tensional stress is released in the low M side, it needs time to accummulate to where it was and then start from there to drag the new near ridge-axis fault away from the ridge-axis while at the

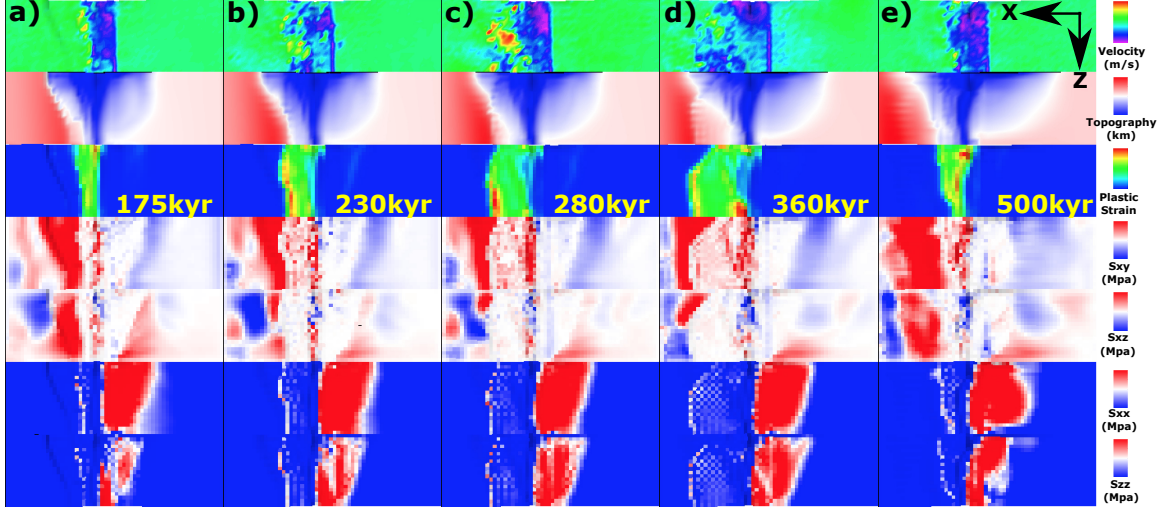


Figure 20: M28SqrtT1 (Table 1). New fault front chase after initial abandoned breakaway.

high M side the increasing tensional stress will directly lead to a fast extending fault front. Thus create the behavior. ^{XT}One question is, how to explain that the fault front is moving much faster than the initial abandoned breakaway? New fault front soon reach the old breakaway. This phenomenon is largely responsible for the corrugations observed. It creates a “X” shape “scan” that first “scan” the topography with faster low M side (Figure 16.d and e) and than with faster high M side (Figure 20.c and d). This results in curved terminations with hundreds to several kilometers wavelengths that directly create parallel to spreading direction corrugations.

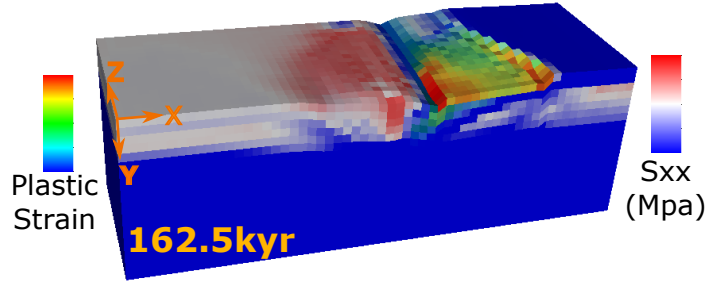


Figure 21: M28SqrtT1 (Table 1). Higher σ_{xx} in the median valley of conjugate plate at low M side.

In addition, the higher σ_{xx} in the median valley of conjugate plate at low M side (Figure 21) is because the brittle crust is thinnest at the median valley, thus when same amount

of force propagates from far field extension to the center median valley, the stress will increases.

3.4 Influence of weakening rate

According to our available twelve 3D models, we have three pairs of models that both have Type one and Type two weakening while the range of M and functional form are maintained to be the same. They are M57(sinoidal), M58(sinoidal) and M58(square root). We will describe their differences respectively.

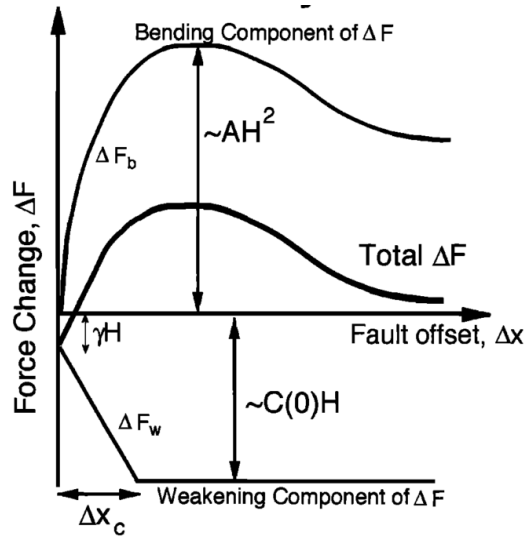


Figure 22: Trade-off between change in bending force ΔF_b and weakening in the fault interface ΔF_w . H is the thickness of the brittle crust and γ is the size of initial weak perturbation and A defines the maximum bending force change. (For more details, please refer to [Lavier et al., 2000])

Before we move on to each of the pairs, the framework studied by [Lavier et al., 2000] needs to be mentioned here for better understanding the model behaviors observed in our model results. There is a trade-off between change in bending force ΔF_b as a function of fault offset ΔX and force change ΔF_w as a function of ΔX due to strain weakening. As described in [Lavier et al., 2000], higher characteristic fault offset (ΔX_c) or slower strain weakening results in multiple faults rather than only one fault lasting. Whether conjugate fault and even multiple faults can be produced depends on the local stress condition. The

strength weakening of the existed fault combines with how much bending force resists the fault to keep offsetting play a major role in determining the stress state at the other areas. As the sea-floor keeps spreading and ΔX increasing, the change in bending force ΔF_b increases and the strength at the fault interface decreases due to weakenging ΔF_w (Figure 22). If the net force change $\Delta F = \Delta F_b + \Delta F_w$ is positive, it means that it is getting harder and harder to maintain the existing fault and stress will begin to accummulate at the other areas which eventually break another fault. ΔF_b initially increases fast with respect to ΔX and then when the breakaway bends over, it reaches its peak value and begin to decreases a little and maintains at a constant value. If the strain weakenging is fast enough that the net effect force ΔF is always negative, then most of the stress will be released by the existing fault and thus no conjugate or multiple faults will be created.

Our model results verify this analysis that only Type two weakening (slower weakening with higher ΔX_c) can produce an alternating normal fault on the conjugate plate.

3.4.1 M57 sinusoidal Type one versus M57 sinusoidal Type two

There are very distinct differences between the two models. They share same functional form (sinusoidal) as well as M range (M57).

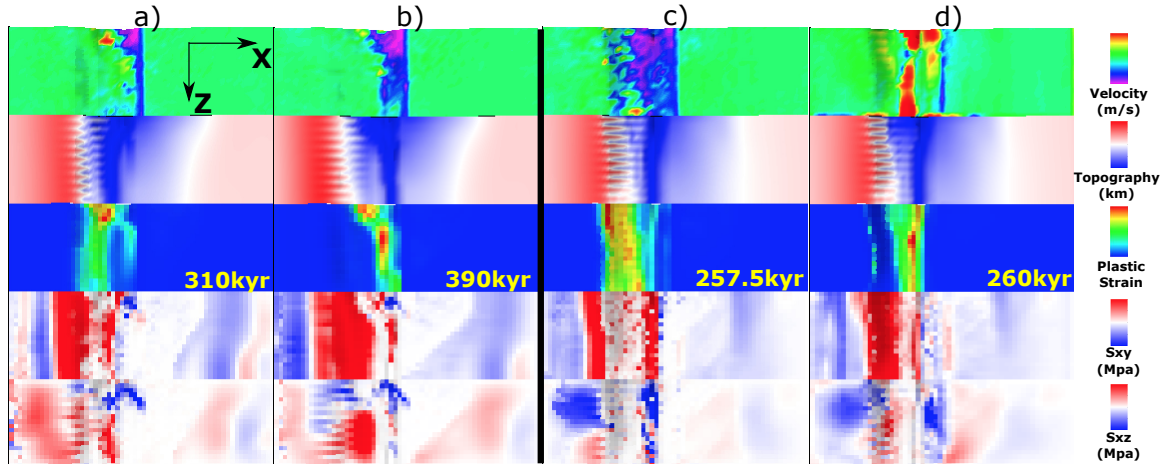


Figure 23: M57SinT2 versus M57SinT1 (Table 1). a) and b) are for M57SinT2, c) and d) are for M57SinT1.

Initially, both models develop normal fault deformations on both sides of the ridge-axis at the low M side. The time for the faults to propagate toward the high M side and cut through the whole crust for M57SinT1 (25kyr) is one half of that for M57SinT2 (50kyr). At around 310kyr, a near axis secondary fault begin to evolve for M57SinT2 at higher M side ($Z > 5$) and soon take the place of initial fault, while at lower M side ($Z \leq 5$), the initial fault remains (Figure 23.a) and b)). However, for M57SinT1, cut back happens around 260kyr and help to maintain a high angle fault with closer to ridge-axis termination. The initial fault remains, no secondary fault forming (Figure 23.a) and b)). In addition, the width of median valley at low M side is wider for M57SinT2 than M57SinT1 (Figure 23.a) and b) versus c) and d)) due to slower weakening (Type two) allows a more distributed tensional stress σ_{xx} rather than fast weakening that once a fault is established, larger amount of tensional stress σ_{xx} will be released at the fault.

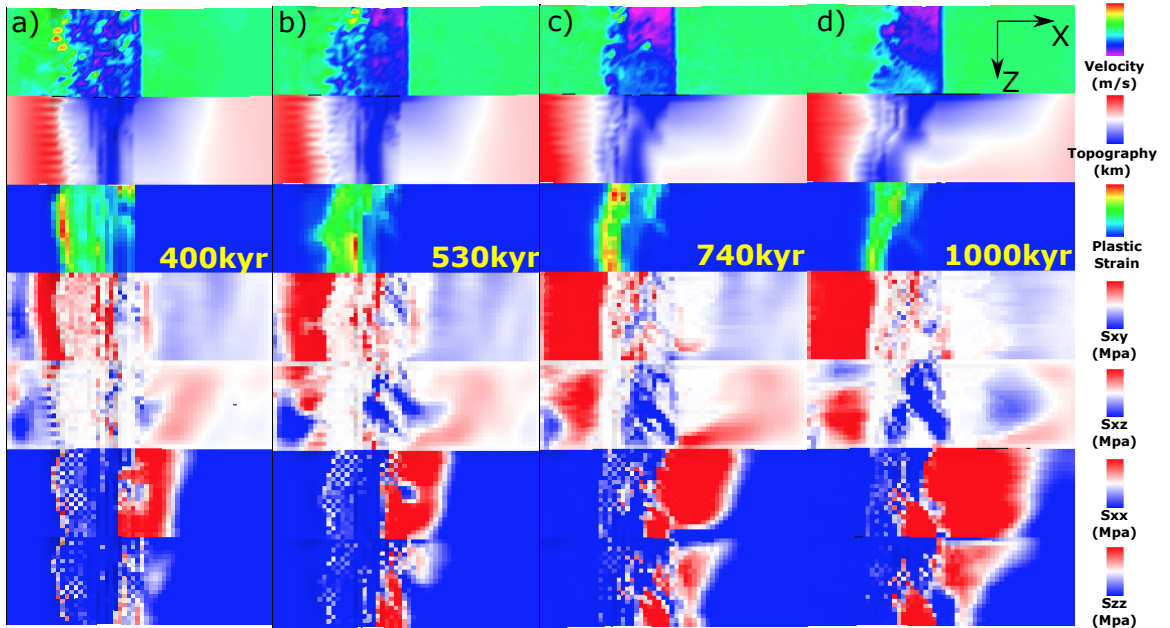


Figure 24: M57SinT1 (Table 1) faulting and stress evolution with respect to time.

M57SinT1 For M57SinT1, as shown in Figure 24, at 400kyr (Figure 24.a), there is opposite dipping normal fault forming at the low M side accommodating part of the extension, which results in a curved termination at the far frontier. As it evolves (530kyr (Figure 24.b)),

the termination at the low M side further recedes backward while the termination at the center ($Z = 11 \sim 13$) extends further. This curved termination leads to a curved topography (white curve in the second row). As the fault evolves and bends further away from the axis, at the time of 740kyr, another opposite dipping normal fault forms again at the low M side (Figure 24.c). It doesn't take the place of initial fault and disappear soon, however, it again releases tensional stress and maintains the termination at far front recede backward. At 1000kyr (Figure 24.d), an Atlantiss Massif shape OCC is produced (low M side (lower magma supply) has a wider dome and high M side (higher magma supply) has a narrower dome) due to the along ridge-axis termination evolution. Corrugations with wavelength varying from hundreds to kilometers are also created.

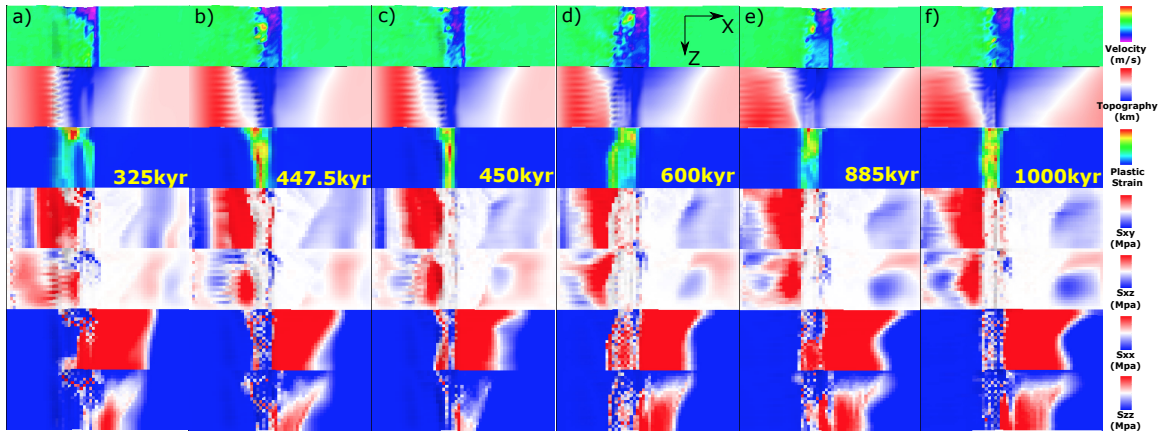


Figure 25: M57SinT2 (Table 1) faulting and stress evolution with respect to time.

M57SinT2 For M57SinT2, as shown in Figure 25, instead of maintaining one fault all the time for M57SinT1, it creates secondary fault at high M side with different mechanism several times. A secondary fault is created at 325kyr (Figure 25.a), when a new near axis normal fault takes the place of the initial one at high M side. Between 447.5kyr (Figure 25.b) and 450kyr (Figure 25.c), termination falls back, and as it evolves, termination at the high M side extends further at 600kyr (Figure 25.d). At 885kyr (Figure 25.e), a secondary fault propagates from low Z to high Z and terminates the further extended fault at high Z and maintains a near ridge-axis termination.

3.4.2 M58SinT1 versus M58SinT2

A major difference between M58SinT1 and M58SinT2 is that M58SinT1 keep faulting at one side of the ridge-axis while M58SinT2's fault alternates.

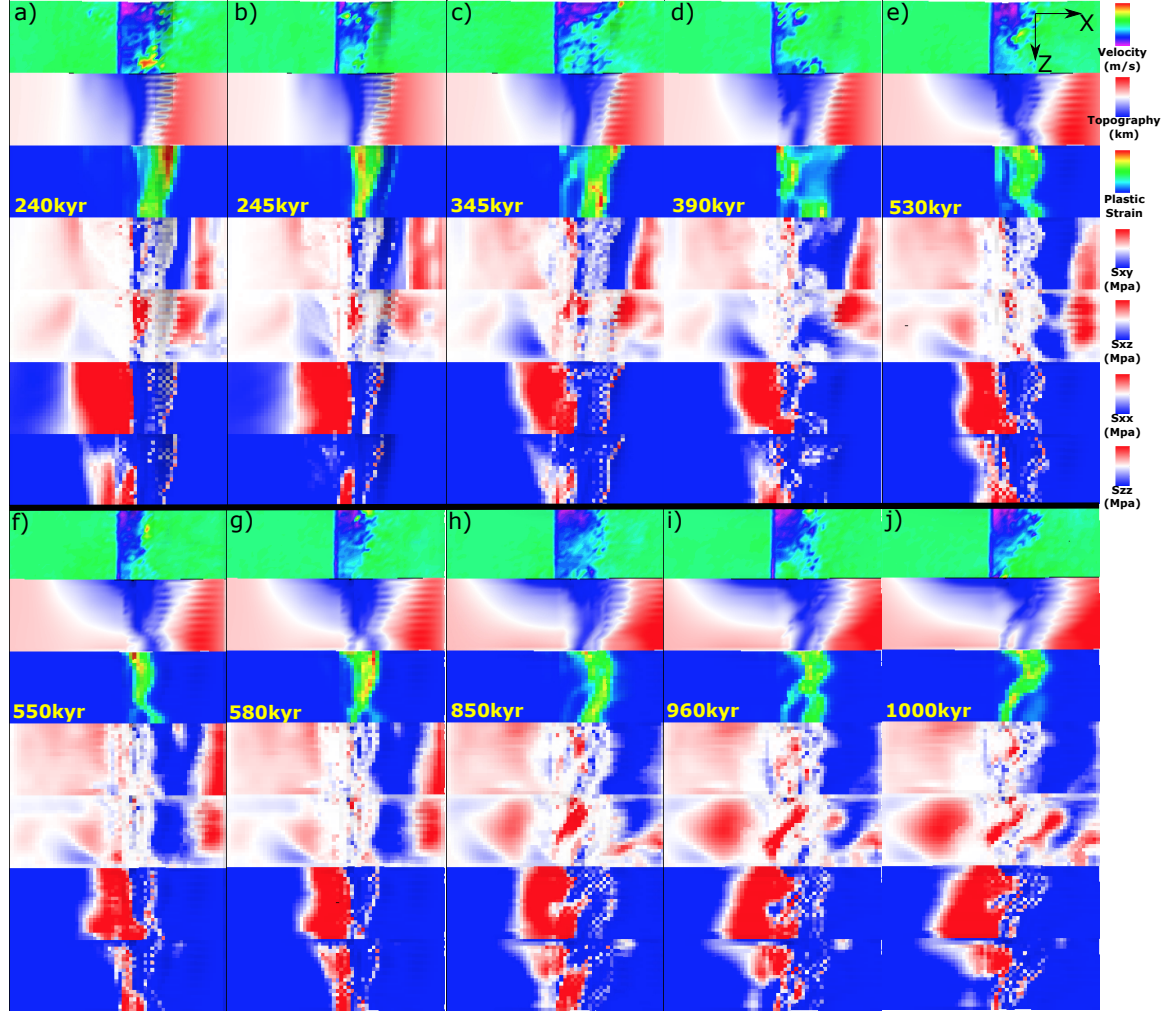


Figure 26: M58SinT1 (Table 1) faulting and stress evolution with respect to time.

M58SinT1 As shown in Figure 26, in 1Myr, the fault keeps on the right hand side of the ridge-axis. It evolves dynamically. Between 240kyr (Figure 26.a) and 245kyr (Figure 26.b), there is a cut back. At 345kyr (Figure 26.c), at low Z side, there are two offsetted antithetic faults ($Z=1 \sim 2$ and $Z=5 \sim 9$) in the hanging wall begin to evolve and soon connect to each other forming anastomosing fault zone. At 390kyr (Figure 26.d), the new

near axis anastomosing fault zone replace the old further away from ridge-axis detachment. There is dextral σ_{xz} forming on the right hand side of the new anastomosing fault zone ((Figure 26.d), row 5) due to the offset between the new near axis fault at low Z side and extended further fault at high Z side and leads to the development of a $\sim 45^\circ$ shear zone connection between the new near axis fault zone at low Z side and the further away from axis original detachment at high Z side. It also creates a curved termination which will lead to a curved topography (boundary between blue and white) seen at 530kyr (Figure 26.e). Note that this curved termination can be a mechanism for producing large wavelength (several kilometers) undulating corrugations. Between 530kyr (Figure 26.e) and 550kyr (Figure 26.f), there is another cut back happens. Terminations fall backwards to near ridge-axis position. At 580kyr (Figure 26.g), at the high Z side, a new near ridge-axis high angle normal fault begin to initiate under the assistance of rotational force from low Z side due to along ridge-axis coupling. This produces a large rider block with several kilometers in its length scale. Previous “S” curved termination now evolves to a half circle curve and it soon affects the curve of topography as seen at 850kyr (Figure 26.h). Due to along ridge-axis variation in diking, a large sinistral shear zone (red region $\sim 40^\circ$ oblique to ridge axis seen in 5th row of 960kyr (Figure 26.i)) keep developing and cut the circle curved fault zone at 850kyr (Figure 26.h) into a new fault zone with higher curvature as seen in 1000kyr (Figure 26.j).

M58SinT2 As shown in Figure 27, the fault initiate on the left hand side of the ridge-axis (Figure 27.a). Low Z side extends further than high Z side. It takes around 100kyr to form into a localized fault plane due to slower rate of weakening. At 215kyr (Figure 27.b), another fault on the conjugate plate begin to evolve and replaces the initial one. As seen from (Figure 27.b), corrugations are created at low Z side. At 330kyr, a third fault forming at the left hand side of the ridge-axis. Between 490kyr (Figure 27.d) and 495kyr (Figure 27.e), there is a cut back.

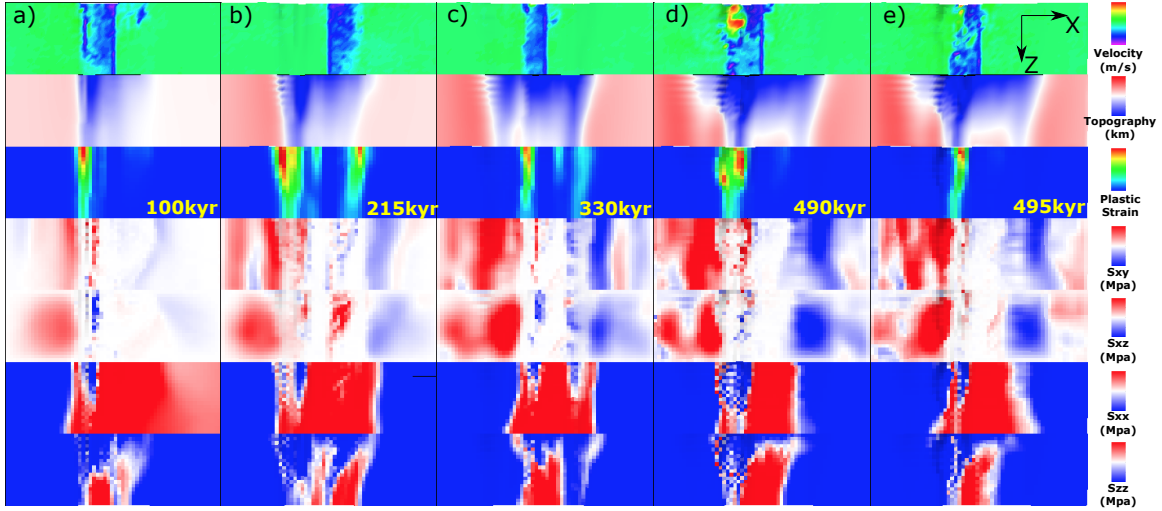


Figure 27: M58SinT2 (Table 1) faulting and stress evolution with respect to time.

3.4.3 M58SqrtT1 versus M58SqrtT2

The major difference between M58SqrtT1 and M58SqrtT2 is also whether the normal fault alternates or not.

M58SqrtT1 As shown in Figure 28, initially, there is a 5 element offset between breakaways along the ridge-axis due to along ridge-axis variation in diking (Figure 28.a). At 370kyr (Figure 28.b), there is a vertical tensile failure at $Z= 1 \sim 2$. Two parallel dextral (blue) shear regions are seen (5th row). The low Z shear zone assists in the shear failure observed at 400kyr (Figure 28.c), and it develops into near ridge-axis normal fault ($Z=4 \sim 12$) and propagates to high Z side which eventually cuts through and reaches $Z= 20$ and replaces the initial extended fault at high Z side at 460kyr (Figure 28.d). The vertical tensile failure zone at $Z= 1 \sim 3$ (Figure 28.d 3rd row) begin to evolve and assists in the initiation of a new near ridge-axis high angle normal fault which connect with the fault at the high Z side (Figure 28.e) at 590kyr. At 660kyr (Figure 28.f 3rd row), there is a hint of high angle normal faulting at $Z= 1 \sim 3$ of conjugate plate. But it doesn't develop. At 730kyr (Figure 28.g 5th row), a dextral (blue) shear zone at the low Z side help to create the faulting pattern seen at 780kyr (Figure 28.h 3rd row), a concave termination with a wavelength of 10

kilometers and it has the potential to create a large wavelength corrugation. Meanwhile, at the low Z side, near the ridge-axis, there is an antithetic fault forming at the hanging wall of the detachment and it later propagates to high Z side (Figure 28.i). From 820kyr to 880kyr, the antithetic fault evolves to near ridge-axis normal fault and connects with the detachment at the high Z side (Figure 28.j). In addition, a tensile failure shows its hint at the low Z side ($Z = 1 \sim 5$) of the conjugate plate.

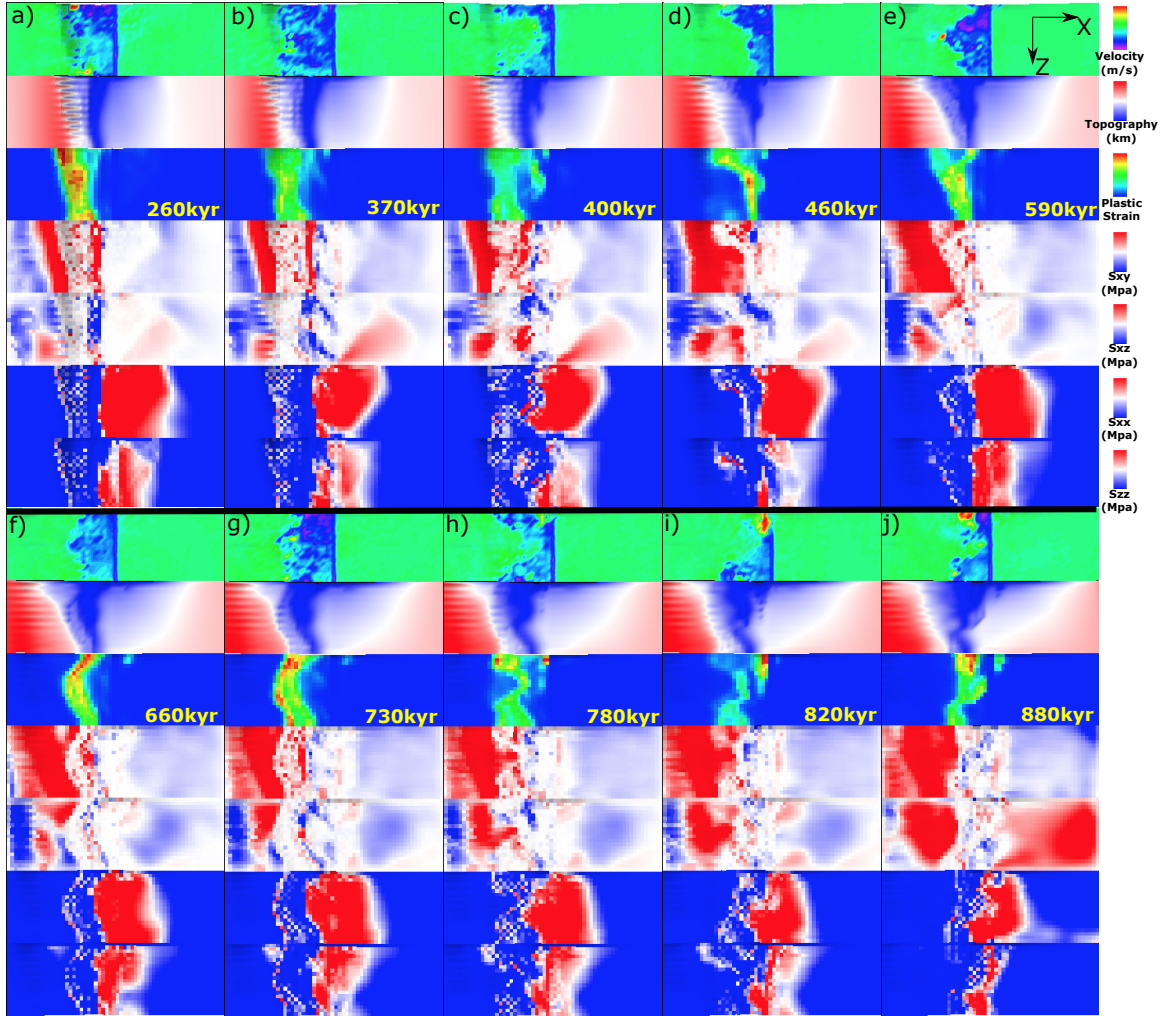


Figure 28: M58SqrtT1 (Table 1) faulting and stress evolution with respect to time.

M58SqrtT2 As shown in Figure 29, at 195kyr (Figure 29.a), due to transtensional stress at low Z side ($Z = 1 \sim 6$), several corrugations begin to evolve. At conjugate plate, dipping toward axis shear zone σ_{xy} (red at 4th row) show its curve and keeps accumulating. σ_{xx}

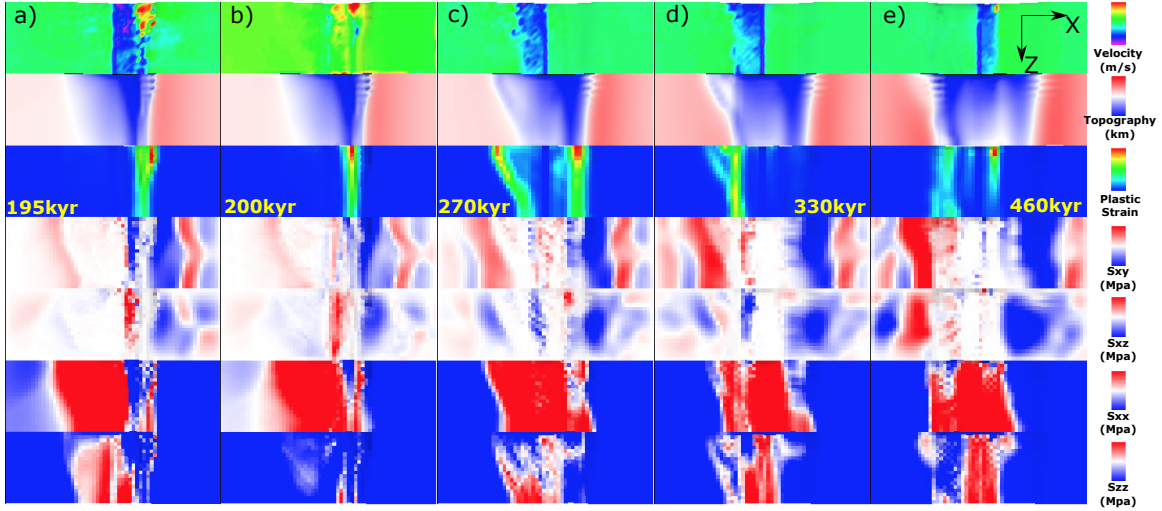


Figure 29: M58SqrtT2 (Table 1) faulting and stress evolution with respect to time.

is also accumulating on the conjugate plate. Between 195kyr (Figure 29.a) and 200kyr (Figure 29.b), there is a cut back. At 270kyr (Figure 29.c), immediately above and following the curved shape shear σ_{xy} zone on the left hand side of the ridge-axis, a new fault begin to evolve and replace the initial fault on the right. At 330kyr (Figure 29.d), at the low Z side, a new near axis high angle normal fault take the place of initial further away from ridge-axis fault partly due to rotational force from along ridge coupling. At 460kyr (Figure 29.e), another normal fault begin to evolve on the right hand side of the ridge-axis.

3.5 Variation of the range of M

So far, we have three ranges for M variations along the ridge-axis (M28, M57 and M58) with same segment length of 20km. Among the 12 available models, two M58 models and the constant $M= 0.8$ model with Type two weakening produce fault alternation while others do not. Generally, M57 and M58 models create a median valley much narrower and shallower than that of M28 models. $\frac{dM}{dz}$ is larger for M28 than M58 and M57.

3.5.1 M28SinT1 versus M57SinT1 versus M58SinT1

M57SinT1 versus M58SinT1 For description of M57SinT1 evolution with respect to time, please refer to Section 3.4.1 and Figure 24. For description of M58SinT1 evolution with respect to time, please refer to Section 3.4.2 and Figure 26. Comparing M57SinT1 and M58SinT1, the major difference is that the faulting pattern evolution for M58SinT1 is much more dynamic with a higher frequency of secondary faults, cut back and offsetted fault segments connection. For M58SinT1, the new secondary near ridge-axis normal or antithetic faults usually replace the existed one. However, for M57SinT1, diking is not strong enough to create big enough stress perturbation along the ridge-axis for secondary or antithetic faults to take the place of the original one. At the low Z side, near ridge-axis antithetic fault only helps to accommodate tensional stress which help maintain a high angle normal fault with near to ridge-axis termination while the termination at the high Z side gradually move off axis. This creates a OCC with larger dome at lower magma supply side than that of higher magma supply side which is opposite to the shape of OCC created by M58SinT1.

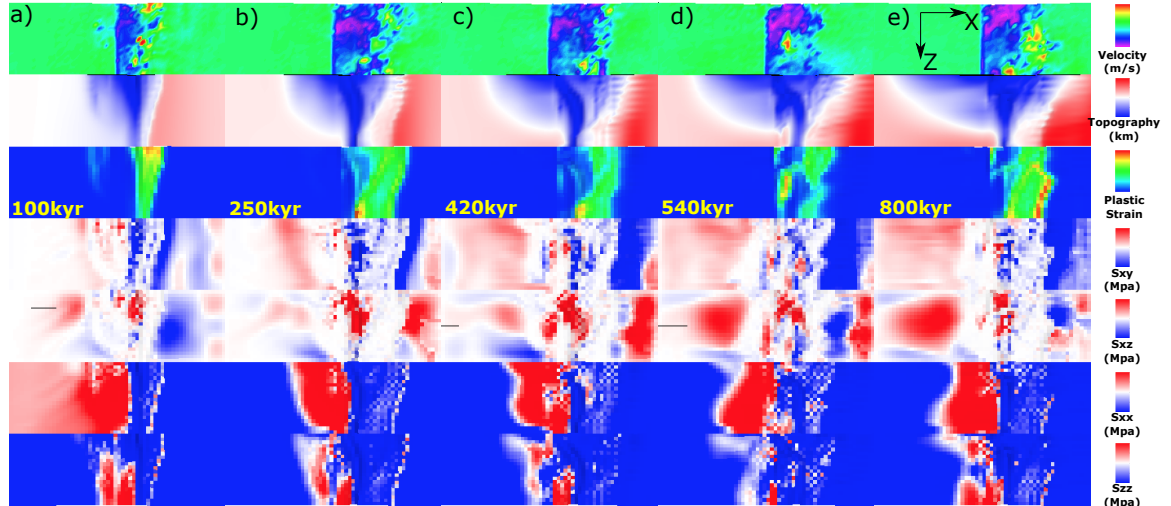


Figure 30: M28SinT1 (Table 1) faulting and stress evolution with respect to time.

M28SinT1 As shown in Figure 30, faulting evolution is much less dynamic than that of M58SinT1. Faulting keeps on the right hand side of the ridge-axis. Only one secondary fault is formed at around 540kyr (Figure 30.d). Initially, at 100kyr (Figure 30.a), at the

low Z side, the normal shear zone at conjugate plate takes up part of the extension and leave a dent in the topography. But it doesn't last long. The initial breakaway of the detachment extends further away from ridge-axis with four elements in along ridge-axis offset at 250kyr (Figure 30.b). At 420kyr, at the high Z side, a hint of new near ridge-axis high angle normal fault begin to show up. It develop into a secondary fault at 540kyr (Figure 30.d) and propagates toward high Z side. This results in a sinistral shear zone (red region in 5th row). At the low Z side ($Z = 1 \sim 3$), a tensile failure can be seen and it take up part of the extension at the low Z side which results in the recede of termination at the low Z side as seen at 800kyr (Figure 30.e) while the termination at higher Z side extends further away from the ridge-axis.

3.5.2 M57SinT2 versus M58SinT2

For description of M57SinT2 evolution with respect to time, please refer to Section 3.4.1 and Figure 25. For description of M58SinT1 evolution with respect to time, please refer to Section 3.4.2 and Figure 27. A major difference is that M57SinT2 does not create alternating normal faults on each side of the ridge-axis while M58SinT2 does. [XT: Why this seemingly small change could lead to such a to the first order difference in model behaviors?](#)

3.5.3 M28LinT1 versus M57LinT1

For description of M28LinT1 evolution with respect to time, please refer to Section 3.1.1.

M57LinT1 As shown in Figure 31, between 160kyr (Figure 31.a) and 162.5kyr (Figure 31.b), there is a cut back. The corrugation is very severe and have a discrete distribution with one element width as its wavelength. The frontier of breakaway also shows discrete distribution of σ_{xx} and σ_{zz} alternating between tension and compression which might be the reason for the undulating topography. At 350kyr (Figure 31.c 3rd row), the two off-

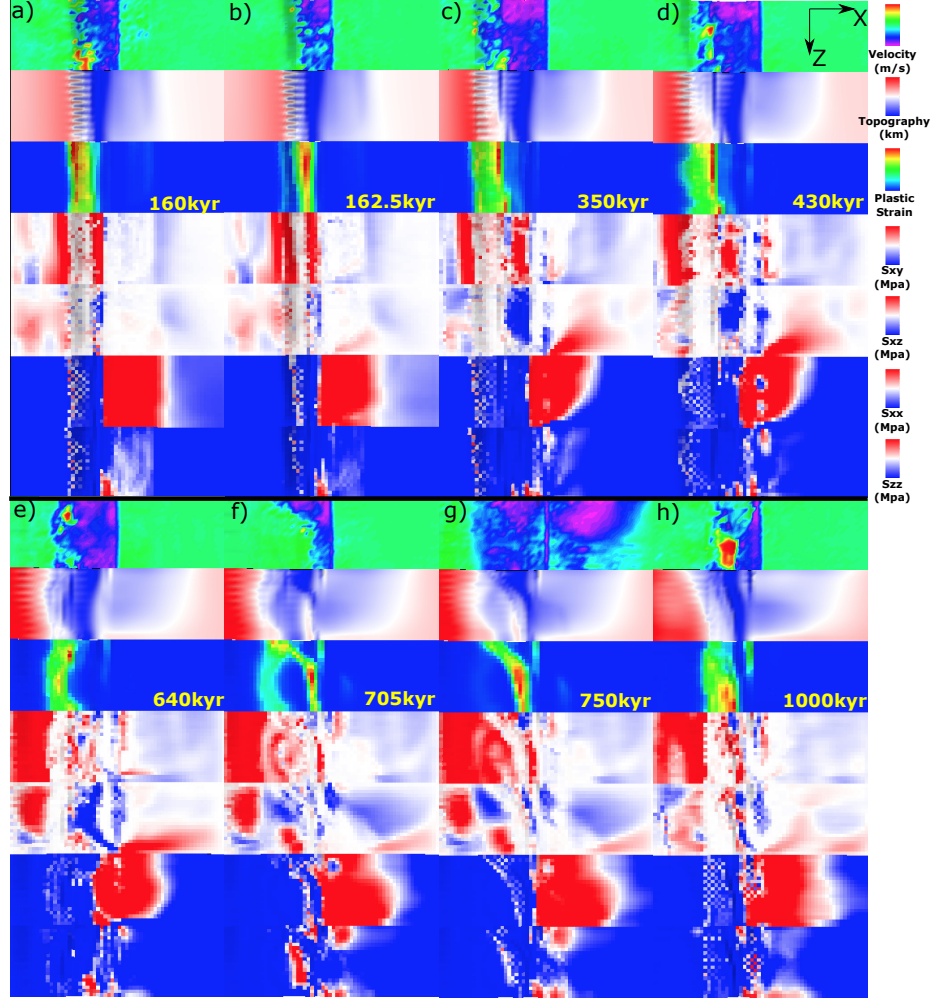


Figure 31: M57LinT1 (Table 1) faulting and stress evolution with respect to time.

setted red line indicates tensile failure at the termination and the shorter one at the high Z side helps maintain a near ridge-axis high angle normal fault. At 430kyr (Figure 31.d), the presence of vertical tensile failure near the ridge-axis at the low Z side is responsible for the recede of the front of the plastic strain at $Z= 1 \sim 3$. While at $Z=5 \sim 10$, the breakaway keeps extending further away from the ridge-axis. This curved front results in a curved topography as seen in 640kyr (Figure 31.e) and is also responsible for the large dextral shear (blue) zone (5th row). At 705kyr (Figure 31.f), a new near ridge-axis secondary fault begin to evolve and replace the original one at high Z side with a length of ~ 15 kilometers. The secondary fault also connect with the further away from ridge-axis original fault at low Z side. The topography at 1000kyr (Figure 31.h) is a result of the curved and later connected

fault. The frontier of the plastic strain at high Z side soon catch up with that at the low Z side due to the presence of a tensile failure zone at the low Z side that has taken up part of the extension.

3.5.4 M28SqrtT1 versus M58SqrtT1

For description of M28SqrtT1 evolution with respect to time, please refer to Paragraph 3.3.1 and Figure 20.

For description of M58SqrtT1 evolution with respect to time, please refer to Paragraph 3.4.3 and Figure 28.

3.5.5 M57SqrtT2 versus M58SqrtT2

For description of M58SqrtT2 evolution with respect to time, please refer to Paragraph 3.4.3 and Figure 29.

M57SqrtT2 As shown in Figure 32

The major difference between M57SqrtT2 and M58SqrtT2 is that M57SqrtT2 keeps faulting at the same side of the ridge-axis while M58SqrtT2 alternates.

3.6 Summary of Findings

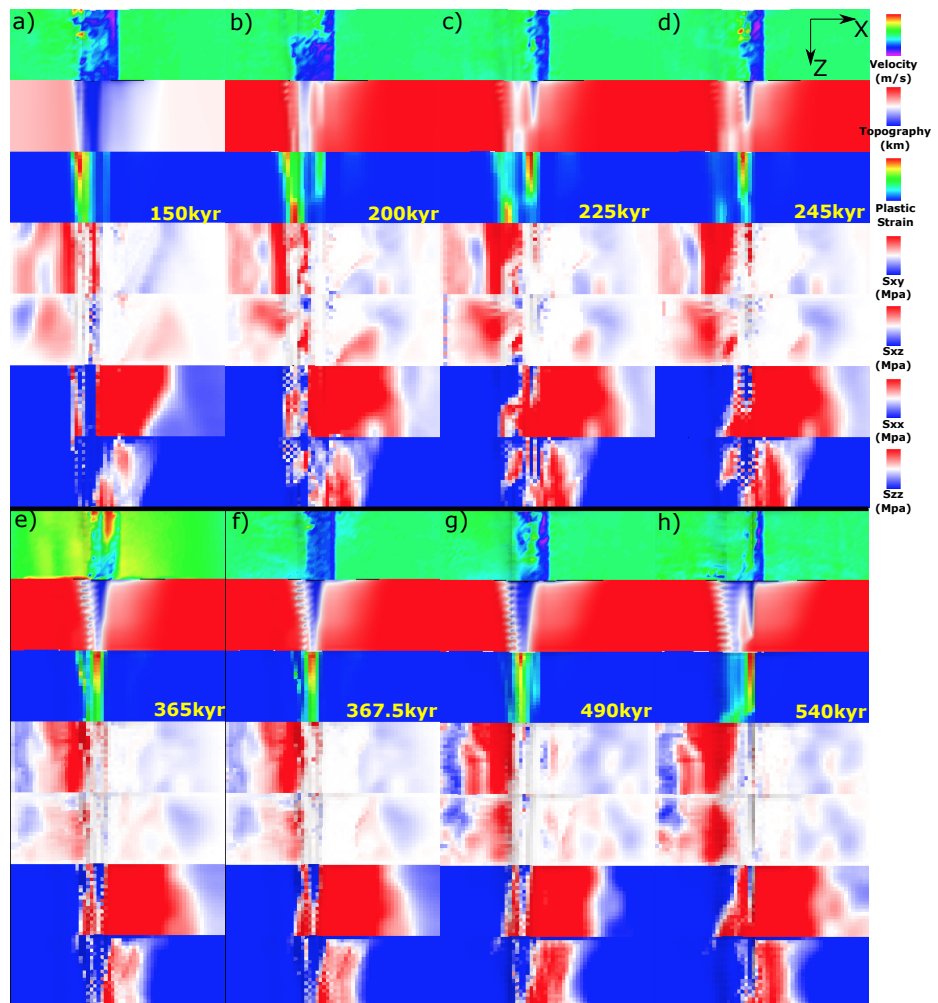


Figure 32: M57SqrtT2 (Table 1) faulting and stress evolution with respect to time.

4 Discussion

Since the model behavior is very complicated. We will focus on the effects being brought by the along ridge-axis variation in diking. Thus, it is worth considering a thought experiment with two end members: One, the along ridge-axis coupling is rigid, so that even along ridge axis variation in M exist, once a fault determined to develop, it will cut through the whole model domain along the ridge-axis(Z-axis) simultaneously. The other end member is that there is totally no coupling along the ridge-axis. So that each slice of crossection profile across the ridge behave separately without being influenced by its neighbour to a extreme that the model behavior is just a combination of 20 pseudo-2D models piled up along ridge-axis with their own M . (IMPORTANT: this suggests the importance and urgence for making clear conclusion and results description for previous pseudo-2D models results. However, one difficulty here is that the characteristic fault offset ΔX_c is different between 2D and 3D models.)

4.1 Discussion of Findings

4.2 Fault alternation

4.2.1 Alternating on conjugate plate

4.2.2 Secondary near-axis normal fault

The secondary near axis high angle normal fault is another common observation of the models. As shown in Figure 8, at the ridge axis with $M > 0.5$ (i.e. $Z > 10$), the existing normal fault will be pushed away from the ridge-axis due to excessive diking, as its mechanism has been mentioned in the introduction chapter, another new near axis normal fault is created at around 650kyr. As it evolve, the initial detachment fault become inactive (the transparent view of plastic strain shown in the rigth corner inset of time 880kyr). This secondary fault creates another dome and its composition is more likely to be volcanic rather

than ultramafic, however, as it evolves, if it can last long, lower crust and upper mantle material can be exhumed to the surface. The composition of the domes observed at Kane magamullions is similar to this mechanism that ultramafic Babel dome is on the West and crustal inside-corner high on the East.

4.2.3 Fault Alternation

The fault alternation behavior observed in pseudo-2D models in cases $M > 0.5$ is much more complicated in 3D models. The results show that only Type two weakening with M58 will result in an alternating faulting pattern. ^{XT:}integrate the area of $M > 0.5$ with respect to Z to see if there is any quantitative analysis available.

4.3 Corrugations

The stress at the tips of the breakaways is generally tensional in both parallel and orthogonal directions to the ridge-axis. (Figure 14.f,g)

4.3.1 Wavelength of corrugations

4.4 Influence of healing

4.5 Comparing model results with nature observation

4.6 Parallel computing efficiency

4.7 Model Limitation

4.7.1 Fixed thermal structure effects and justification

Thermal conduction rate for $\kappa = 6 \text{ mm}^2/\text{s}$ material is $1.8 \times 10^5 \text{ km/Myr}$, four magnitude faster compared to spreading rate of 2.5 km/Myr .

4.8 Reccommendation for Future Research

References

- G. Baines, M. J. Cheadle, B. E. John, and J. J. Schwartz. The rate of oceanic detachment faulting at atlantis bank, sw indian ridge. *Earth and Planetary Science Letters*, 273(1-2):105–114, Aug. 2008. ISSN 0012821X. doi: 10.1016/j.epsl.2008.06.013.
- R. Buck, L. Lavier, and A. Poliakov. Modes of faulting at mid-ocean ridges. *Nature*, 434(7034):719–23, 2005. ISSN 1476-4687. doi: 10.1038/nature03358.
- S. M. Carbotte, D. K. Smith, M. Cannat, and E. M. Klein. Tectonic and magmatic segmentation of the global ocean ridge system : a synthesis of observations. *Geological Society of London*, 2015.
- Y. J. Chen and J. Lin. Mechanisms for the formation of ridge-axis topography at slow-spreading ridges: A lithospheric-plate flexural model. *Geophysical Journal International*, 136:8–18, 1999. ISSN 0956540X. doi: 10.1046/j.1365-246X.1999.00716.x.
- E. Choi, L. Lavier, and M. Gurnis. Thermomechanics of mid-ocean ridge segmentation. *Physics of the Earth and Planetary Interiors*, 171(1-4):374–386, Dec. 2008. ISSN 00319201. doi: 10.1016/j.pepi.2008.08.010.
- C. M. R. Fowler. *The solid earth: an introduction to global geophysics*. Cambridge University Press, 2004.
- S. Kirby and A. K. Kronenberg. Rheology of the lithosphere: Selected topics. *Reviews of Geophysics*, 25(6):1219–1244, 1987.
- L. L. Lavier, W. R. Buck, and A. N. B. Poliakov. Factors controlling normal fault offset in an ideal brittle layer. *Journal of Geophysical Research*, 105(B10):23431, 2000. doi: 10.1029/2000JB900108.
- J. Lin, G. M. Purdy, H. Schouten, J.-C. Sempere, and C. Zervas. Evidence from gravity

data for focused magmatic accretion along the Mid-Atlantic Ridge. *Nature*, 344:627–632, 1990. ISSN 0028-0836. doi: 10.1038/344627a0.

W. B. F. Ryan, S. M. Carbotte, J. O. Coplan, S. O’Hara, A. Melkonian, R. Arko, R. A. Weissel, V. Ferrini, A. Goodwillie, F. Nitsche, J. Bonczkowski, and R. Zemsky. Global multi-resolution topography synthesis. *Geochemistry, Geophysics, Geosystems*, 10, 2009. ISSN 15252027. doi: 10.1029/2008GC002332.

D. K. Smith, H. Schouten, H. J. B. Dick, J. R. Cann, V. Salters, H. R. Marschall, F. Ji, D. Yoerger, A. Sanfilippo, R. Parnell-turner, C. Palmiotto, A. Zhelezov, H. Bai, W. Junkin, B. Urann, S. Dick, M. Sulanowska, P. Lemmond, and S. Curry. Development and evolution of detachment faulting along 50 km of the mid-atlantic ridge near 16.5°n. *Geochemistry Geophysics Geosystems*, pages 4692–4711, 2014. doi: 10.1002/2014GC005563. Received.

M. Tolstoy, A. J. Harding, and J. A. Orcutt. Crustal Thickness on the Mid-Atlantic Ridge: Bull’s-Eye Gravity Anomalies and Focused Accretion. *Science*, 262(October):726–729, 1993. ISSN 0036-8075. doi: 10.1126/science.262.5134.726.

B. E. Tucholke, M. D. Behn, W. R. Buck, and J. Lin. Role of melt supply in oceanic detachment faulting and formation of megamullions. *Geology*, 36(6):455, 2008. ISSN 0091-7613. doi: 10.1130/G24639A.1.

D. L. Turcotte and G. Schubert. *Geodynamics*. Cambridge, 2002.